impressive overall performance for water oxidation, reaching a photocurrent density of 2.8 ± 0.2 mA/cm^2 at 0.6 V versus RHE (Fig. 3A and table S2), which is markedly better than those of $BiVO_4$/FeOOH and $BiVO_4$/NiOOH and is almost comparable with the performance of bare $BiVO_4$ for sulfite oxidation.

When NiOOH was first deposited on the $BiVO_4$ surface and FeOOH was added as the outermost layer to form $BiVO_4$/NiOOH/FeOOH (reversed OEC junction), the resulting E_{FB}s determined by sulfite photocurrent onset (fig. S9A and table S3) and Mott-Schottky plot (fig. S10 and table S4) are comparable with those of $BiVO_4$/FeOOH, again confirming that the E_{FB} of the $BiVO_4$ photoanode is affected by the pH_{PZZP} of the outermost OEC. Also, the *J-V* curve for sulfite oxidation by $BiVO_4$/NiOOH/FeOOH was comparable with that by $BiVO_4$/NiOOH, confirming that a $BiVO_4$/NiOOH junction is not favorable for interface recombination (Fig. 3, C and E). As a result, $BiVO_4$/NiOOH/FeOOH shows the lowest photocurrent for water oxidation. These results prove that the photocurrent enhancement achieved by the $BiVO_4$/FeOOH/NiOOH photoanode for photoelectrolysis of water is truly due to the simultaneous optimization of the $BiVO_4$/OEC and OEC/electrolyte junctions, using an optimum dual OEC structure.

The applied bias photon-to-current efficiency (ABPE) of the $BiVO_4$/FeOOH/NiOOH electrode calculated by using its *J-V* curve, assuming 100% Faradaic efficiency, is plotted in Fig. 4A (*35*). The maximum ABPE of 1.75% achieved by the system is impressive because it is obtained by using unmodified $BiVO_4$ as a single photon absorber. Moreover, this efficiency is achieved at a potential as low as 0.6 V versus RHE, which is a highly favorable feature for assembling a tandem cell or a photoelectrochemical diode (*12*, *36*, *37*). The ABPE obtained by using a two-electrode system (working electrode and a Pt counter electrode), which achieves the maximum ABPE of 1.72%, is also shown in fig. S11 (*35*). The long-term stability of $BiVO_4$/FeOOH/NiOOH was tested by obtaining a *J-t* curve. A photocurrent density of 2.73 mA/cm^2, obtained by applying 0.6 V between the working and counter electrodes, was maintained for 48 hours without showing any sign of decay, proving its long-term stability (Fig. 4B). The O_2 measurement made by using a fluorescence O_2 sensor confirmed that the photocurrent generated at 0.6 V versus counter-electrode was mainly associated with O_2 production (> 90% photocurrent-to-O_2 conversion efficiency) (Fig. 4C). The same results were obtained when the measurement was performed at 0.6 V versus RHE. H_2 production at the Pt counter electrode was also detected with gas chromatography (GC) (Fig. 4C). The molar ratio of the produced H_2:O_2 was 1.85:1. The slight deviation from the stoichiometric ratio of 2:1 is due to our imperfect manual sampling method of H_2 for GC analysis.

Because this outstanding performance was achieved by using simple, unmodified $BiVO_4$ (no extrinsic doping and no composition tuning) as the only photon absorber, further improvement of the cell efficiency is expected when various strategies of tuning compositions or forming heterojunctions and tandem cells are used to enhance photon absorption and electron-hole separation.

References and Notes

1. A. Kudo, K. Omori, H. Kato, *J. Am. Chem. Soc.* **121**, 11459–11467 (1999).
2. Y. Park, K. J. McDonald, K.-S. Choi, *Chem. Soc. Rev.* **42**, 2321–2337 (2013).
3. Y. Liang, T. Tsubota, L. P. A. Mooij, R. van de Krol, *J. Phys. Chem. C* **115**, 17594–17598 (2011).
4. F. F. Abdi, R. van de Krol, *J. Phys. Chem. C* **116**, 9398–9404 (2012).
5. F. F. Abdi, T. J. Savenije, M. M. May, B. Dam, R. van de Krol, *J. Phys. Chem. Lett* **4**, 2752–2757 (2013).
6. D. K. Zhong, S. Choi, D. R. Gamelin, *J. Am. Chem. Soc.* **133**, 18370–18377 (2011).
7. H. S. Park *et al.*, *J. Phys. Chem. C* **115**, 17870–17879 (2011).
8. W. J. Jo *et al.*, *Angew. Chem. Int. Ed. Engl.* **51**, 3147–3151 (2012).
9. S. P. Berglund, A. J. E. Rettie, S. Hoang, C. B. Mullins, *Phys. Chem. Chem. Phys.* **14**, 7065–7075 (2012).
10. K. Zhang, X. J. Shi, J. K. Kim, J. H. Park, *Phys. Chem. Chem. Phys.* **14**, 11119–11124 (2012).
11. Y. Park, D. Kang, K.-S. Choi, *Phys. Chem. Chem. Phys.* **16**, 1238–1246 (2014).
12. F. F. Abdi *et al.*, *Nat. Commun* **4**, 2195 (2013).
13. K. J. McDonald, K.-S. Choi, *Energy Environ. Sci* **5**, 8553–8557 (2012).
14. T. Allen, *Particle Size Measurement* (Chapman and Hall, London, 1997).
15. J. A. Seabold, K.-S. Choi, *J. Am. Chem. Soc.* **134**, 2186–2192 (2012).
16. R. Sarala, M. A. Islam, S. B. Rabin, D. M. Stanbury, *Inorg. Chem.* **29**, 1133–1142 (1990).
17. D. M. Stanbury, *Adv. Inorg. Chem.* **33**, 69–138 (1989).
18. J.-F. Reber, K. Meier, *J. Phys. Chem.* **88**, 5903–5913 (1984).
19. H. Dotan, K. Sivula, M. Grätzel, A. Rothschild, S. C. Warren, *Energy Environ. Sci* **4**, 958–964 (2011).
20. J. M. Foley, M. J. Price, J. I. Feldblyum, S. Maldonado, *Energy Environ. Sci* **5**, 5203–5220 (2012).
21. M. Zhou *et al.*, *ChemSusChem* **5**, 1420–1425 (2012).
22. A. J. E. Rettie *et al.*, *J. Am. Chem. Soc.* **135**, 11389–11396 (2013).
23. L. Trotochaud, J. K. Ranney, K. N. Williams, S. W. Boettcher, *J. Am. Chem. Soc.* **134**, 17253–17261 (2012).
24. R. D. L. Smith *et al.*, *Science* **340**, 60–63 (2013).
25. M. W. Louie, A. T. Bell, *J. Am. Chem. Soc.* **135**, 12329–12337 (2013).
26. C. Y. Cummings, F. Marken, L. M. Peter, A. A. Tahir, K. G. Wijayantha, *Chem. Commun. (Camb.)* **48**, 2027–2029 (2012).
27. L. M. Peter, K. G. Wijayantha, A. A. Tahir, *Faraday Discuss.* **155**, 309–322, discussion 349–356 (2012).
28. J. Nozik, *Annu. Rev. Phys. Chem.* **29**, 189–222 (1978).
29. S. R. Morrison, in *Electrochemistry at Semiconductor and Oxidized Metal Electrodes* (Plenum Press, New York, 1980), pp. 49–78.
30. N. C. Castillo, A. Heel, T. Graule, C. Pulgarin, *Appl. Catal. B* **95**, 335–347 (2010).
31. S. Obregón, G. Colón, *J. Mol. Catal. Chem.* **376**, 40–47 (2013).
32. R. M. Cornell, U. Schwertmann, *The Iron Oxides: Structure, Properties, Reactions, Occurrences and Uses* (Wiley VCH, New York, 2003).
33. D. M. Sherman, *Geochim. Cosmochim. Acta* **69**, 3249–3255 (2005).
34. N. Hernández, R. Moreno, A. J. Sánchez-Herencia, J. L. Fierro, *J. Phys. Chem. B* **109**, 4470–4474 (2005).
35. Z. Chen *et al.*, *J. Mater. Res.* **25**, 3–16 (2010).
36. M. G. Walter *et al.*, *Chem. Rev.* **110**, 6446–6473 (2010).
37. L. Tong *et al.*, *Energy Environ. Sci* **5**, 9472–9475 (2012).

Acknowledgments: We acknowledge support from the Center for Chemical Innovation of the National Science Foundation (POWERING THE PLANET: grant CHE-1305124). We thank M. A. Woo for electrodepositing FeOOH and NiOOH on FTO substrates and testing their electrochemical water oxidation performances.

Supplementary Materials

www.sciencemag.org/content/343/6174/990/suppl/DC1
Materials and Methods
Figs. S1 to S11
Tables S1 to S4
References (*38*–*41*)

7 October 2013; accepted 31 January 2014
Published online 13 February 2014;
10.1126/science.1246913

A Direct Quantitative Measure of Surface Mobility in a Glassy Polymer

Y. Chai,[1] T. Salez,[3] J. D. McGraw,[4]* M. Benzaquen,[3] K. Dalnoki-Veress,[3,4] E. Raphaël,[3] J. A. Forrest[1,2]†

Thin polymer films have striking dynamical properties that differ from their bulk counterparts. With the simple geometry of a stepped polymer film on a substrate, we probe mobility above and below the glass transition temperature T_g. Above T_g the entire film flows, whereas below T_g only the near-surface region responds to the excess interfacial energy. An analytical thin-film model for flow limited to the free surface region shows excellent agreement with sub-T_g data. The system transitions from whole-film flow to surface localized flow over a narrow temperature region near the bulk T_g. The experiments and model provide a measure of surface mobility in a simple geometry where confinement and substrate effects are negligible. This fine control of the glassy rheology is of key interest to nanolithography among numerous other applications.

The last decades have seen a considerable interest in the dynamical and rheological properties of glassy materials (*1*, *2*). Recent efforts (*1*, *3*–*5*) have focused on elucidating the nature of glassy dynamics both in the bulk and in systems, such as thin films or colloids,

where the interfaces play a dominant role and can induce strong dynamical heterogeneities. Higher mobility near interfaces has often been suggested as the cause of anomalous glass transition temperature (T_g) in thin polymer films (*3*–*5*). The presence of a more mobile surface has practical implications for thin-film coatings related to lubrication, wear, and friction. Flow on a near-surface layer can also place strict lower limits on feasible length scales for nanolithography (*6*–*8*). Although earlier investigations provided some contradictory conclusions (*9*, *10*), most recent reports are consistent with a region of enhanced mobility on the surface of glassy polymer films. There have also been reports of enhanced surface mobility in small-molecule glasses (*11*, *12*). The parallels between polymeric and small-molecule glasses suggest that enhanced surface mobility is a more general property of glass-forming materials. Most current research efforts have a goal of providing a quantitative description, including the temperature dependence, of the properties of the near-surface region. Surface response to nanoparticle embedding has been used to probe anomalous surface dynamics in both polymeric and small-molecule glasses (*13*–*17*). That work showed that small molecules can flow on the surface, whereas larger polymers have enhanced segmental mobility but do not flow owing to their larger molecular size. Relaxation of an imposed surface topography has been used to demonstrate enhanced mobility in polymeric (*18*–*21*) and small-molecule systems (*11*). For small-molecule glasses, the enhanced surface mobility is often discussed in terms of surface diffusion (*22*), where the molecules at the free surface have a diffusion time that can be orders of magnitude smaller than the bulk value (*11*, *12*). For polymers, the most complete description comes from studies of low-molecular-weight polystyrene (*23*).

The use of capillary leveling as a probe of rheology on the nanometer scale (*24*–*26*) has been successfully used to study polymer rheology for films at temperatures much greater than the T_g value of the polymer. Stepped films were annealed, and a decrease in the surface area was monitored to probe dissipation of the system's free energy, with a complete quantification of the rheological properties (*24*–*26*). The low-molecular-weight films considered here are sufficiently thin that gravitational effects can be ignored, yet thick enough that van der Waals interactions resulting in a disjoining pressure can be neglected. Gradients in the curvature of the free surface result in Laplace pressure gradients that drive viscous flows. When the height gradients are sufficiently small, and the typical height of the profile is sufficiently smaller than its typical width, the flow can be described by the Stokes equations in the lubrication approximation (*27*). For homogenous viscous films, the evolution of the profile $h(x,t)$ is described by the capillary-driven thin-film equation (TFE) (*28*)

$$\partial_t h + \frac{\gamma}{3\eta_b}\partial_x(h^3\partial_x^3 h) = 0 \qquad (1)$$

where η_b is the bulk viscosity, γ is the surface tension, x is the horizontal coordinate, and t is the time. The TFE can be solved numerically for a stepped initial profile (*25*), and the solution has been shown to converge in time toward a self-similar profile in the variable $xt^{-1/4}$.

For the case of films with $T < T_g$, the majority of the film is unable to flow. Because previous studies have shown an evolution of the free surface to minimize surface area and energy in polymeric (*18*, *19*) and nonpolymeric glasses (*12*, *17*), there must be some flow localized over a thin layer near the free surface. At a given temperature, we will assume the thickness h_m of this mobile layer, with viscosity η_m, to be constant (see Fig. 1B). Of course, the present two-layer model is an approximation, and one would expect a continuous variation from surface to bulk dynamics through the sample (*29*). However, this simple description provides a first-order approach with a single free parameter, as shown below. Invoking Stokes equations in the lubrication approximation for the surface layer, and assuming no slip between the glassy and surface layers and no shear at the free surface, leads to

$$\partial_t h + \frac{\gamma h_m^3}{3\eta_m}\partial_x^4 h = 0 \qquad (2)$$

which we will refer to as the glassy thin-film equation (GTFE). It is mathematically identical to the linearized TFE. The GTFE thus has an exact analytical solution for a stepped initial profile (*26*), which is self-similar in the variable $xt^{-1/4}$. This solution can be used to extract a single free parameter describing the flow: $\gamma h_m^3/3\eta_m$. The form of Eq. 2 is mathematically identical to the Mullins model (*22*) describing the evolution of profiles by surface diffusion of molecules. However, for flow of macromolecules where all the segments must move together, the GTFE interpretation in terms of surface flow in a layer of size h_m is more relevant than this collective surface diffusion scenario. Figure 1 displays a schematic diagram of the two flow regimes studied. The first is for $T > T_g$ with homogeneous viscosity (TFE), and the second for $T < T_g$, where there is only a thin layer of mobile fluid atop an immobile glassy film (GTFE). The self-similar nature of both Eqs. 1 and 2 implies that, by fitting their solutions to the experimental profiles, one can determine the physical quantities of the problem through a single free parameter. This method of investigation can be carried out with films thick enough that chain confinement and polymer-substrate effects can be ignored.

Films were prepared by spin-coating from a dilute solution of polystyrene (PS) dissolved in toluene onto two types of substrates: silicon (Si) with the native oxide layer, and freshly cleaved mica substrates. The PS had weight-averaged molecular weight $M_w = 3.0$ kg mol^{-1}, and polydispersity index 1.09 (Polymer Source Inc., Dorval, Québec). Samples were annealed at 348 K, which is 5 K above bulk T_g, in an oven flushed with dry N_2 for 12 hours. Films with thickness h_2 on mica substrates were floated onto the surface of purified water in order to separate the films from the mica. The previously coated Si substrates, coated with PS of thickness h_1, were then dipped into the water and used to pick up the floating films. These low-molecular-weight films are fragile when floating on the water surface and break into smaller sections with several straight vertical edges. Thus, when transferred, these "float-gaps" form perfect steps of height h_2 over bottom films of height h_1 (see Fig. 1A). The dilatometric T_g of independent, annealed flat films on Si was measured by ellipsometry. For $h \geq 40$ nm, we found $T_g = 343 \pm 2$ K.

We first demonstrate that the stepped film samples level at temperatures much less than the

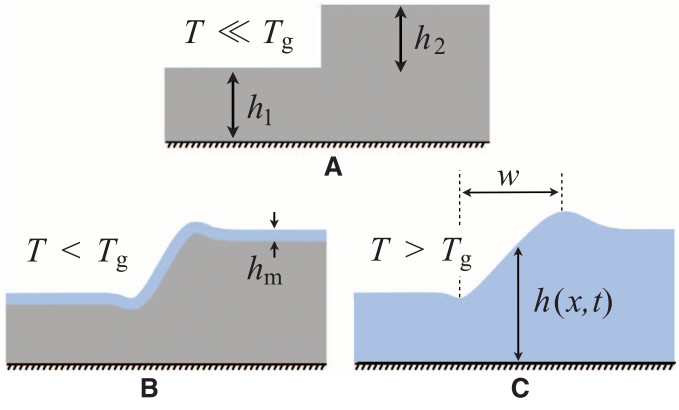

Fig. 1. Schematic diagram of the simple geometry and flow regions. (**A**) An as-prepared sample at room temperature. (**B** and **C**) The two flow mechanisms discussed in the paper. (**C**) describes the evolution of the total height profile $h(x,t)$ through whole-film flow (TFE) (see Eq. 1), and (**B**) shows the evolution of the total height profile through flow localized in a small region near the free surface (GTFE) (see Eq. 2). The flow region is indicated in blue and is assumed to vanish far below T_g.

[1]Department of Physics and Astronomy and Guelph-Waterloo Physics Institute, University of Waterloo, Waterloo, Ontario N2L 3G1, Canada. [2]Perimeter Institute for Theoretical Physics, 31 Caroline Street North, Waterloo, Ontario N2L 2Y5, Canada. [3]Laboratoire de Physico-Chimie Théorique, UMR CNRS Gulliver 7083, École Supérieure de Physique et de Chimie Industrielles (ESPCI), Paris, France. [4]Department of Physics and Astronomy, McMaster University, Hamilton, Ontario L8S 4M1, Canada.

*Present address: Department of Experimental Physics, Saarland University, 66041 Saarbrücken, Germany.
†Corresponding author. E-mail: jforrest@uwaterloo.ca

bulk T_g. We performed a simple width evolution experiment where three types of stepped polymer films were prepared with the same bottom-layer thickness, h_1 = 90 nm, and top-layer thicknesses of h_2 = 14, 23, and 42 nm (see Fig. 1A). The stepped films were collectively heated in a N_2 filled oven and removed after various annealing times for measurement at room temperature with atomic force microscopy (AFM) (JPK Instruments, Berlin). Scan lines were averaged to produce a profile, and the width w (see Fig. 1C) was obtained by fitting this profile to a tanh[x/(w/2)] function. Figure 2A shows the temporal evolution of w for this series of stepped films at five different temperatures. There is an increase with time of the width at temperatures as much as 30 K below the bulk T_g value. This indicates enhanced mobility in the glassy film. Furthermore, as suggested by both Eqs. 1 and 2, the width varies as $w = (at)^{1/4}$ at all temperatures, where a is a factor that depends a priori on temperature and initial geometry. This 1/4 power law demonstrates the existence of a capillary-driven flow both above and below T_g. By analogy with the scaling analysis of Stillwagon and Larson (*30*), a simple determination of the effective viscosity η_{eff} of the sample can be obtained by the vertical offset between the lines in Fig. 2A, using $\eta_{eff} \propto a^{-1}$. The effective viscosity corresponds to the viscosity of the sample calculated as if flow occurs in the entire film, within the lubrication approximation. For a given geometry, it is then possible to compare the η_{eff} values obtained at all temperatures to one, η_0, at a particular reference temperature T_0, to get a relative measure of the effective viscosity of the entire film. Setting $T_0 = T_g$, Fig. 2B shows the relative effective viscosity, $\eta_{eff}/\eta_0 = a_0/a$, for all film geometries. The solid line in this plot is the Vogel-Fulcher-Tammann (VFT) law for PS (*31*). When $T > T_g$, the temperature dependence of the effective viscosity agrees quantitatively with the bulk VFT law. However, for $T < T_g$, there is significant deviation away from this line. There are two ways in which this difference can be interpreted: Either (i) the entire film flows with viscosity reduced below that predicted by the VFT law (either because the viscosity is reduced from the bulk one or because the bulk viscosity deviates from the VFT law for $T < T_g$), or (ii) the assumption of whole-film flow is invalid.

To distinguish between these two possibilities, we turn to a more quantitative investigation based on the TFE and GTFE. Stepped polymer films with $h_1 = h_2 = 90$ nm were used. Typically, AFM images were collected over a square region of size ~1 μm by 1 μm for glassy samples and up to ~50 μm by 50 μm for melt samples. This measurement was repeated until the shape of the profile was self-similar in the variable $xt^{-1/4}$ or, for cases of the two temperatures in the transition region, until a sample was heated for a total of 90 hours. All AFM measurements were carried out at room temperature. For the TFE (see Eq. 1) and GTFE (see Eq. 2), the long-time solutions have been shown to be self-similar in the variable $xt^{-1/4}$ (*24*–*26*). Therefore, if we plot the film height $h(x,t)$ as a function of $xt^{-1/4}$ for several times, the profiles should superimpose. Figure 3, A and B, shows a number of measured profiles over a large time window, both for temperatures below T_g (left) and above T_g (right). Figure 3, C and D, shows that the profiles are indeed self-similar. Although the data obeys this self-similarity for $T < T_g$ and $T > T_g$, there are important differences between the two temperature regimes. In particular, the shapes of the self-similar profiles are different. See, for example, Fig. 3, C and D, where one can see that above T_g the magnitude of the bump (first top oscillation) is larger than that of the dip (first bottom oscillation). Below T_g, it is similarly evident that the bump and dip extrema are equal in magnitude. To be more precise, above T_g these features depend quantitatively on h_1 and h_2, whereas below T_g the surface flows without sensitivity to the substrate for the considered thicknesses. In the latter case, samples with same h_2 but different h_1 show bumps and dips that are all equal in magnitude (fig. S1). This simple qualitative feature of the profiles shows that it is the surface alone that flows below T_g. Fits of the sub-T_g profiles to solutions of both the TFE and GTFE quantitatively highlight the differences. The left plots of Fig. 3 are for $T < T_g$. The blue solid line in Fig. 3C is a best fit of the self-similar experimental profile to the GTFE analytical solution (*26*). The residuals of the fit are also shown as a blue solid line in Fig. 3E. The red dashed line in Fig. 3E corresponds to the fit of the sub-T_g data to the TFE numerical solution (*25*). In the sub-T_g case, the experimental profiles are thus much better described by the GTFE than by the TFE, as the residuals are much lower and do not exhibit the systematic variation seen in the dashed residuals. Similarly, the experimental data on the right side of Fig. 3 are for $T > T_g$ and are much better represented by the TFE than by the GTFE.

Because the TFE and GTFE correspond to different physical pictures, we can define a single metric, χ, for the goodness of fit to each model. χ is used to characterize the transition from where the system is best described by whole-film flow to where it is best described by surface flow over thickness h_m. We define this quantity by the correlation function

$$\chi = \frac{\int dx (h_{EXP} - h_{TFE})^2}{\int dx (h_{GTFE} - h_{TFE})^2} \quad (3)$$

where h_{EXP} is the self-similar experimental profile, h_{TFE} is the numerical solution (*25*) of the TFE, and h_{GTFE} is the analytical solution (*26*) of the GTFE. This function equals 1 if the experimental data are exactly described by the GTFE solution and 0 if the experimental data are exactly described by the TFE solution. Figure 4 shows the temperature dependence of χ as well as the temperature dependence of the thermal expansivity dh/dT derived from ellipsometry measurements for an independent flat 87-nm-thick film. This type of ellipsometry data is often used to find the dilatometric T_g value in thin films (*4*), and in this case gives rise to $T_g = 343 \pm 2$ K. It is remarkable that $\chi(T)$ undergoes an abrupt transition at a temperature indistinguishable from the bulk T_g value. This means that the system undergoes

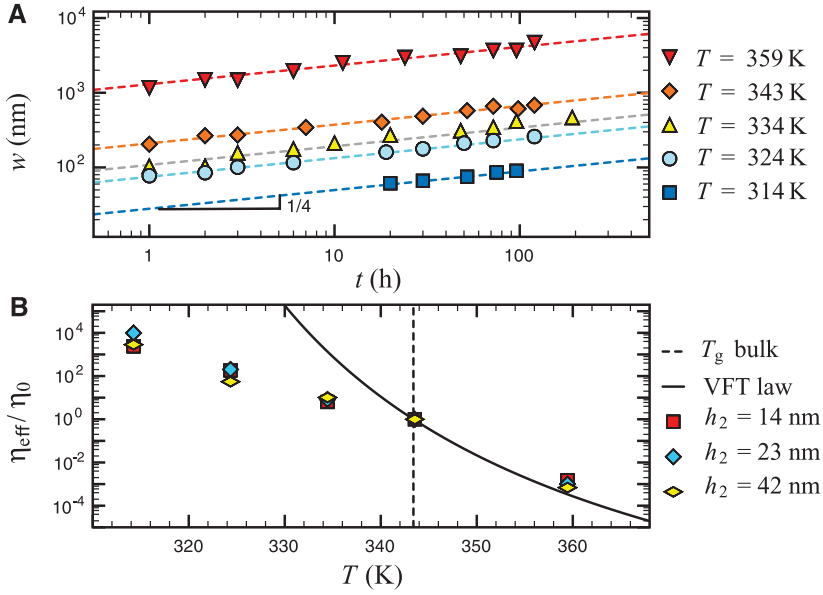

Fig. 2. Temporal evolution of the width of stepped films and temperature dependence of the effective viscosity. (**A**) The temporal evolution of the width w (see Fig. 1C), obtained by fitting the profile to a tanh[x/(w/2)] function, for h_1 = 90 nm and h_2 = 42 nm, at temperatures near the bulk T_g = 343 K. The dashed lines have slope 1/4. (**B**) Effective viscosities (see definition in text) normalized to the one at $T_0 = T_g$ for a given geometry, for films with h_1 = 90 nm and h_2 as indicated. Errors are comparable to the symbol size.

a sharp transition from bulk flow to surface-dominated flow as the temperature is lowered through the bulk T_g value. The transition temperature should be interpreted as the one below which most of the film exhibits no flow on the 90-hour time scale.

Polystyrene is a model glass-forming material, and through our measurements, we should be able to probe other aspects of the glassy dynamics. In particular, while the data shown in Fig. 4 are for profiles having reached steady state or after 90 hours of annealing, whichever occurs first, we can measure the time dependence of the shape of the profile at temperatures near the transition. For temperatures in this range, we might expect to see evidence of the time-dependent mechanical properties of the glassy material. In particular, glass-forming materials behave like elastic solids on short time scales and like viscous materials on much larger time scales. We thus might expect that for short times the system would behave like a glassy material, with flow only occurring in the surface region and the profile well described by the GTFE, and for long times the system would be well characterized by flow of the entire film with a profile well described by the TFE. The inset shows the temporal evolution of χ for the particular 343 K and 348 K data, which lie in the transition region. For the case of $T = 343$ K, the initial χ value is near 1, meaning that the system is initially dominated by flow localized in a surface region. As the system evolves in time, this correlation decreases, and the system becomes less well described by the GTFE. The sample at $T = 348$ K shows even more striking behavior. In this case, one can see that over a period of 3×10^5 s the system goes from being well described by flow localized in the surface region ($\chi \sim 1$), to being well described by flow in the entire film ($\chi \sim 0$). In this transition region, because the shape of the profile is changing from glass-like to fluid-like, the profiles cannot be self-similar over a large time window.

The time dependences of χ at $T = 343$ and 348 K show that the height profiles can be used to monitor the system as it changes from glass-like to liquid-like behavior. This also implies that we could probe in a single sample more than one temperature, as long as we waited for the profile to reach a self-similar state at each temperature. The data shown with diamond symbols in Fig. 4 show that a single sample, with a film thickness large enough so that chain confinement and substrate effects can safely be neglected, can exhibit a transition from bulk flow to surface flow. This thickness range can also be used for molecular glasses where other experiments requiring thinner films would not be appropriate, because dewetting is too rapid above T_g.

The numerical fits to the data can be used to extract meaningful physical parameters. In both the TFE and GTFE cases, there is a single free horizontal stretching parameter that determines the fit of the self-similar experimental profile to the dimensionless theoretical solution. Knowing the tabulated (*32*) surface tension γ, the GTFE fitting parameter (see Eq. 2) gives the surface mobility $h_m^3/(3\eta_m)$, and the TFE fitting parameter (see Eq. 1) gives the bulk viscosity η_b. As a more direct comparison, we plot the GTFE mobility $h_m^3/(3\eta_m)$ and the average TFE mobility $\left(h_1 + \frac{h_2}{2}\right)^3/(3\eta_b)$ on the single composite plot of Fig. 5. The result is consistent with that of Yang *et al.* (*23*) but with two differences in the methodology: We use films that are thick enough to prevent chain confinement and substrate effects, and we have the possibility of using a single sample to obtain the entire curve. The solid line is obtained from using the bulk VFT law for PS of the same M_w (*31*). The agreement we obtain for $T > T_g$ (left side of Fig. 5) is consistent with the previous success of the stepped-film technique in polymer melts (*24*). Of more importance for the present work is the sub-T_g mobility (right side of Fig. 5), for which we observe a strong deviation from the bulk VFT law. In this temperature range, the single-fit parameter $h_m^3/(3\eta_m)$ combines the two relevant physical quantities of the mobile surface layer: its size and viscosity. Using reasonable constraints, we now estimate each parameter individually. For any flow to occur, the size of the surface region has to be large enough so that the polymer molecules fit into it. Molecules larger than the surface region size will have segments in the glassy region and will thus be unable to flow. For PS with $M_w = 3$ kg mol^{-1}, the root-mean-squared end-to-end distance of the molecule satisfies $\langle R_{EE}\rangle_{RMS} \sim 3$ nm, and we can use this as a first estimate for the surface region size that is similar to the one in (*33*, *34*). This length scale coupled with the data in Fig. 5 suggests a surface viscosity of $\eta_m \sim 2 \times 10^8$ Pa · s at 323 K. We note that we used only an estimate for h_m, and the subsequent estimated value of η_m is very sensitive to this chosen thickness. In particular, the constraint $h_m > \langle R_{EE}\rangle_{RMS}$ may be too strong, as this is an average of the molecular size, and it is only necessary that there is a significant fraction of the molecules that have all segments in the surface region in order to have surface flow. Alternatively, if we used the value of $h_m \sim 1$ nm suggested as a lower limit in (*17*), we would predict a surface viscosity of 7.7×10^6 Pa · s at 323 K, which is 20 K below T_g. This surface viscosity is more than 3 orders of magnitude lower than the bulk viscosity at T_g. Finally, the observed linear trend (in log-lin scale) of Fig. 5 below T_g allows us to infer an Arrhenius behavior of the surface mobility below T_g, with

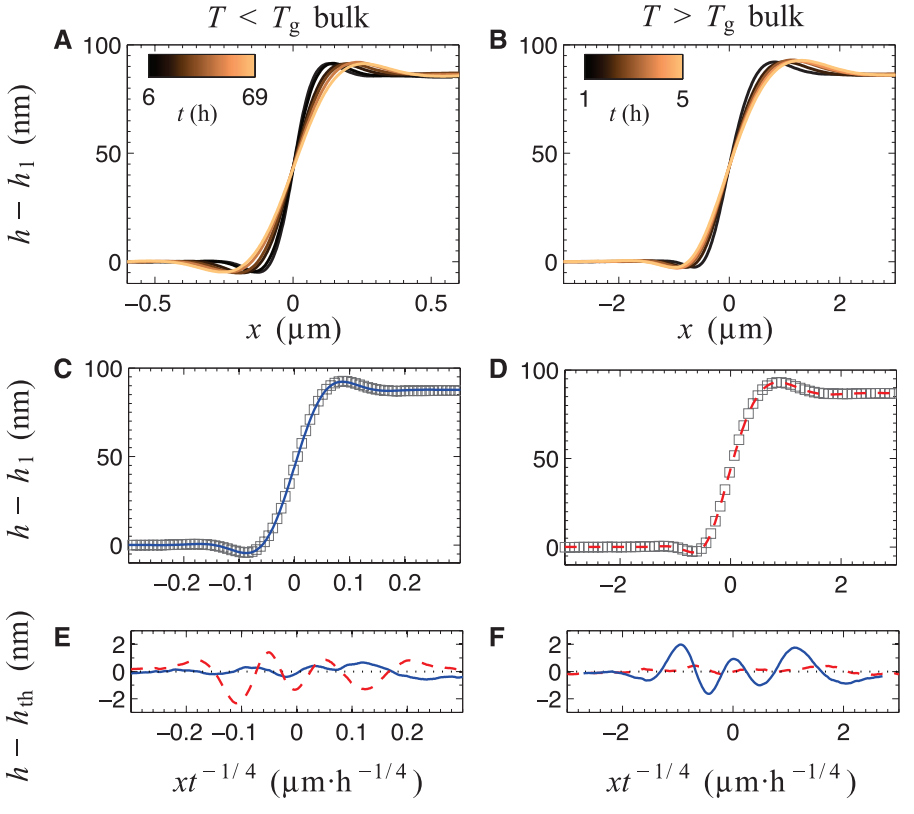

Fig. 3. Height profiles and fits below and above T_g. In both the glassy (left) ($T = 333$ K) and melt (right) ($T = 353$ K) cases, the top (**A** and **B**) shows the temporal evolutions of experimental profiles with $h_1 = h_2 = 90$ nm; the center (**C** and **D**) are the collapsed experimental profiles (white squares) showing self-similar behavior in the variable $xt^{-1/4}$; and the bottom (**E** and **F**) demonstrates the goodness of fit of each collapsed profile to either the TFE numerical solution or the GTFE analytical solution. In (C), (D), (E), and (F), the blue solid line corresponds to the GTFE and the red dashed line corresponds to the TFE.

activation energy $E_a \sim 337 \pm 20$ kJ mol^{-1}, in agreement with existing literature (*18*, *20*, *23*).

In conclusion, by employing the stepped-film geometry and analyzing the resulting flow, we report quantitative evidence for the existence of a thin layer of liquid-like material at the free surface of glassy, low-molecular-weight polystyrene films. The sample thicknesses and preparation are such that annealing effects, chain confinement, and substrate effects can be neglected. The transition from whole-film flow to flow localized in a thin surface layer has been measured and observed to occur sharply at the bulk T_g value. For temperatures inside the transition region, we were able to measure time-dependent evolutions from glassy to liquid behavior. This technique provides an opportunity to accurately follow the transition from surface flow to bulk flow within a single sample. Below T_g, a fit to the measured profile gives a surface mobility parameter $h_m^3/(3\eta_m)$ that can be used to estimate a surface viscosity. In particular, we obtain $\eta_m \sim 10^8$ Pa · s at 20 K below T_g. Independent determination of either the size $h_m(T)$ of the surface region or its viscosity $\eta_m(T)$ would allow a complete determination of the temperature-dependent properties of the near-surface region.

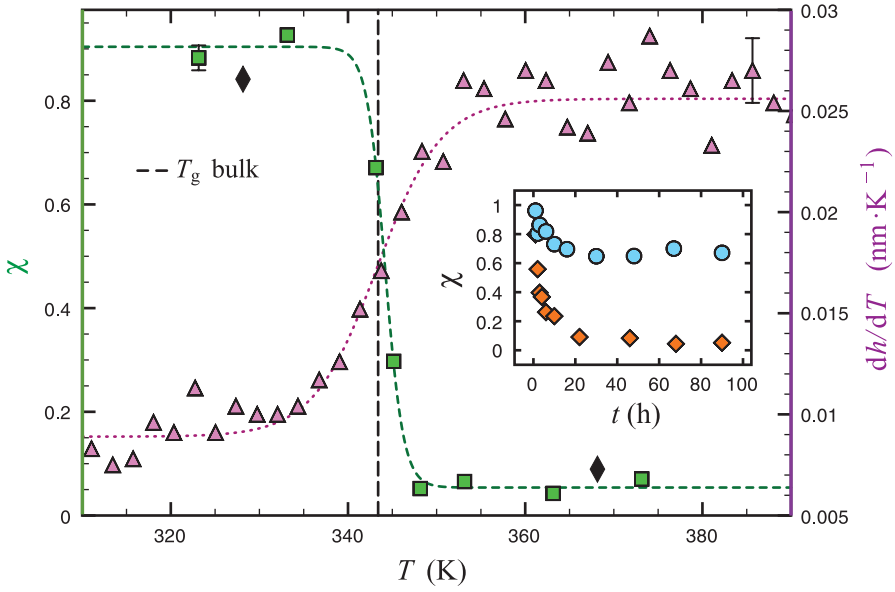

Fig. 4. Temperature dependence of the correlation function and thermal expansivity. The correlation function $\chi(T)$ defined in Eq. 3 is given by the green square and black diamond symbols (left axis) for samples with $h_1 = h_2 = 90$ nm. The thermal expansivity for an independent flat 87-nm sample is given by the purple triangles (right axis). The black diamond symbols are $\chi(T)$ for a single sample that was held first for 90 hours at $T < T_g$, then measured and heated to $T > T_g$ until the self-similar profile was reached. The inset shows the temporal evolution of χ for $T = 343$ K and 348 K data that lie in the transition region (blue circles are for $T = 343$ K; orange diamonds are for $T = 348$ K). Error bars are indicated once for each subplot.

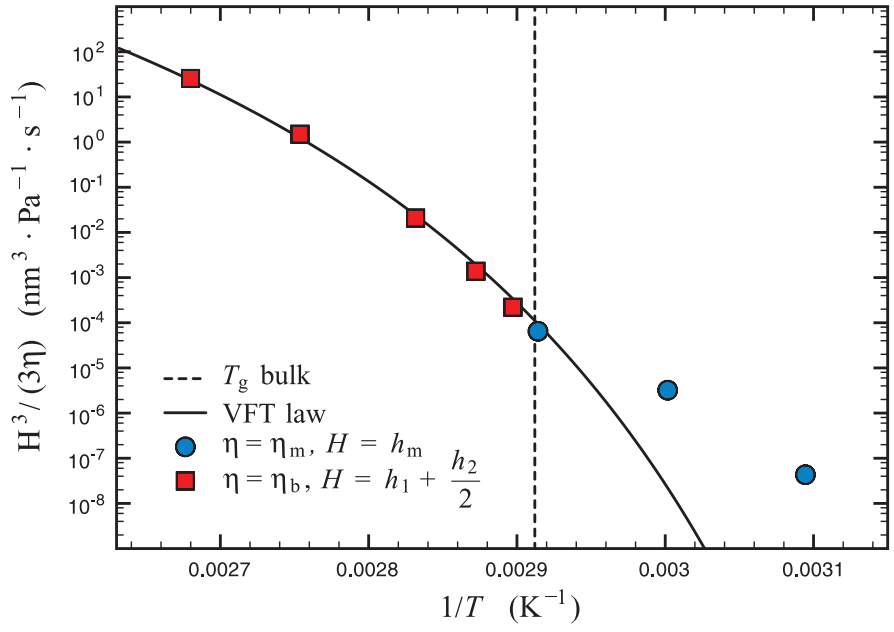

Fig. 5. Temperature dependence of the mobility. This figure is made of two subplots representing $h_1 = h_2 = 90$-nm samples. The mobility $H^3/(3\eta)$ is determined by a fit to either the analytical GTFE solution (blue circles) or the numerical TFE solution (red squares), with η and H as defined in the legend.

References and Notes

1. M. D. Ediger, P. Harrowell, *J. Chem. Phys.* **137**, 080901 (2012).
2. P. W. Anderson, *Science* **267**, 1615–1616 (1995).
3. J. A. Forrest, *Eur. Phys. J. E* **8**, 261–266 (2002).
4. J. A. Forrest, K. Dalnoki-Veress, *J. Coll. Int. Sci.* **94**, 167–195 (2001).
5. M. Alcoutlabi, G. B. McKenna, *J. Phys. Condens. Matter* **17**, R461–R524 (2005).
6. J. Teisseire, A. Revaux, M. Foresti, E. Barthel, *Appl. Phys. Lett.* **98**, 013106 (2011).
7. E. Rognin, S. Landis, L. Davoust, *Phys. Rev. E Stat. Nonlin. Soft Matter Phys.* **84**, 041805 (2011).
8. E. Rognin, S. Landis, L. Davoust, *J. Vac. Sci. Technol. B* **30**, 011602 (2012).
9. T. Kerle, Z. Lin, H. Kim, T. P. Russell, *Macromolecules* **34**, 3484–3492 (2001).
10. S. Ge *et al.*, *Phys. Rev. Lett.* **85**, 2340–2343 (2000).
11. L. Zhu *et al.*, *Phys. Rev. Lett.* **106**, 256103 (2011).
12. R. Malshe, M. D. Ediger, L. Yu, J. J. de Pablo, *J. Chem. Phys.* **134**, 194704 (2011).
13. J. H. Teichroeb, J. A. Forrest, *Phys. Rev. Lett.* **91**, 016104 (2003).
14. M. Ilton, D. Qi, J. A. Forrest, *Macromolecules* **42**, 6851–6854 (2009).
15. D. Qi, M. Ilton, J. A. Forrest, *Eur. Phys. J. E* **34**, 56 (2011).
16. D. Qi, Ph.D. thesis, University of Waterloo, Ontario, Canada, 2009.
17. C. R. Daley, Z. Fakhraai, M. D. Ediger, J. A. Forrest, *Soft Matter* **8**, 2206 (2012).
18. Z. Fakhraai, J. A. Forrest, *Science* **319**, 600–604 (2008).
19. D. Qi, Z. Fakhraai, J. A. Forrest, *Phys. Rev. Lett.* **101**, 096101 (2008).
20. R. M. Papaléo *et al.*, *Phys. Rev. B* **74**, 094203 (2006).
21. E. Buck, K. Petersen, M. Hund, G. Krausch, D. Johannsmann, *Macromolecules* **37**, 8647–8652 (2004).
22. W. W. Mullins, *J. Chem. Phys.* **30**, 77 (1959).
23. Z. Yang, Y. Fujii, F. K. Lee, C.-H. Lam, O. K. C. Tsui, *Science* **328**, 1676–1679 (2010).
24. J. D. McGraw, T. Salez, O. Bäumchen, E. Raphaël, K. Dalnoki-Veress, *Phys. Rev. Lett.* **109**, 128303 (2012).
25. T. Salez *et al.*, *Eur. Phys. J. E* **35**, 114 (2012).
26. T. Salez, J. D. McGraw, O. Bäumchen, K. Dalnoki-Veress, E. Raphaël, *Phys. Fluids* **24**, 102111 (2012).
27. Materials and methods are available as supplementary materials on *Science* Online.
28. R. Blossey, *Thin Liquid Films: Dewetting and Polymer Flow* (Springer, Dordrecht, 2012).
29. J. A. Forrest, *J. Chem. Phys.* **139**, 084702 (2013).
30. L. E. Stillwagon, R. G. Larson, *J. Appl. Phys.* **63**, 5251 (1988).
31. J.-C. Majeste, J.-P. Montfort, A. Allal, G. Marin, *Rheol. Acta* **37**, 486–499 (1998).
32. S. Wu, *J. Chem. Phys.* **74**, 632–638 (1970).
33. J. Mattsson, J. A. Forrest, L. Borjesson, *Phys. Rev. E Stat. Phys. Plasmas Fluids Relat. Interdiscip. Topics* **62**, (4 Pt B), 5187–5200 (2000).

34. J. A. Forrest, J. Mattsson, *Phys. Rev. E Stat. Phys. Plasmas Fluids Relat. Interdiscip. Topics* **61**, R53–R56 (2000).

Acknowledgments: The authors acknowledge the École Normale Supérieure of Paris, the Fondation Langlois, the Chaire Total–ESPCI ParisTech, as well as the Natural Sciences and Engineering Research Council of Canada, for financial support. We also thank O. Bäumchen for interesting discussions.

Supplementary Materials
www.sciencemag.org/content/343/6174/994/suppl/DC1
Materials and Methods
Figs. S1 and S2
Database S1
References (*35*, *36*)

19 August 2013; accepted 3 February 2014
10.1126/science.1244845

Rapid Thinning of Pine Island Glacier in the Early Holocene

J. S. Johnson,[1]*† M. J. Bentley,[2,1]† J. A. Smith,[1] R. C. Finkel,[3,4] D. H. Rood,[3,5]‡ K. Gohl,[6] G. Balco,[7] R. D. Larter,[1] J. M. Schaefer[8,9]

Pine Island Glacier, a major outlet of the West Antarctic Ice Sheet, has been undergoing rapid thinning and retreat for the past two decades. We demonstrate, using glacial-geological and geochronological data, that Pine Island Glacier (PIG) also experienced rapid thinning during the early Holocene, around 8000 years ago. Cosmogenic ^{10}Be concentrations in glacially transported rocks show that this thinning was sustained for decades to centuries at an average rate of more than 100 centimeters per year, which is comparable with contemporary thinning rates. The most likely mechanism was a reduction in ice shelf buttressing. Our findings reveal that PIG has experienced rapid thinning at least once in the past and that, once set in motion, rapid ice sheet changes in this region can persist for centuries.

Ice mass loss from the Pine Island–Thwaites sector dominates the contemporary contribution to sea level from the West Antarctic Ice Sheet (WAIS) (*1*, *2*). Pine Island Glacier (PIG) (Fig. 1A) in particular is currently experiencing considerable acceleration, thinning, and retreat (*3*–*6*). This has raised concerns over how much ice will be lost to the ocean before the ice stream stabilizes (*5*–*8*). Satellite altimetry measurements show an increase in rates of thinning of ice close to the PIG grounding line from 1.2 to 6 m year^{-1} between 2002 and 2007 (*4*, *9*). In addition, thinning has been detected 150 km upstream of the grounding line (*10*). The pattern of change is best explained by a dynamic response to increased influx of warm water to the cavity under the ice shelf at the glacier front (*11*–*14*). However, the record of change—and our understanding of dynamic changes—over longer time scales of centuries to millennia is still limited. Consequently, there is considerable uncertainty associated with model projections of the future evolution of PIG and hence the rate and timing of future ice loss (*15*). The geological record provides evidence of styles and rates of past ice sheet change that can provide constraints on the bounds of possible future change (*16*). In the PIG region, the existing geological record consists largely of marine geological data describing grounding line retreat across the continental shelf (*17*–*21*). In contrast, little is known about the terrestrial thinning

[1]British Antarctic Survey, Natural Environment Research Council, High Cross, Madingley Road, Cambridge CB3 0ET, UK. [2]Department of Geography, Durham University, South Road, Durham DH1 3LE, UK. [3]Center for Accelerator Mass Spectrometry, Lawrence Livermore National Laboratory, Post Office Box 808 L-397, Livermore, CA 94550, USA. [4]Earth and Planetary Science Department, University of California, Berkeley, CA 94720, USA. [5]Earth Research Institute, University of California, Santa Barbara, CA 93106, USA. [6]Alfred Wegener Institute Helmholtz–Centre for Polar and Marine Research, Am Alten Hafen 26, 27568 Bremerhaven, Germany. [7]Berkeley Geochronology Center, 2455 Ridge Road, Berkeley, CA 94709, USA. [8]Lamont-Doherty Earth Observatory (LDEO), Columbia University, Route 9W, Palisades, NY 10964, USA. [9]Department of Earth and Environmental Sciences, Columbia University, New York, NY 10027, USA.

*Corresponding author. E-mail: jsj@bas.ac.uk
†These authors contributed equally to this work.
‡Present address: Scottish Universities Environmental Research Centre, Rankine Avenue, Scottish Enterprise Technology Park, East Kilbride G75 0QF, UK.

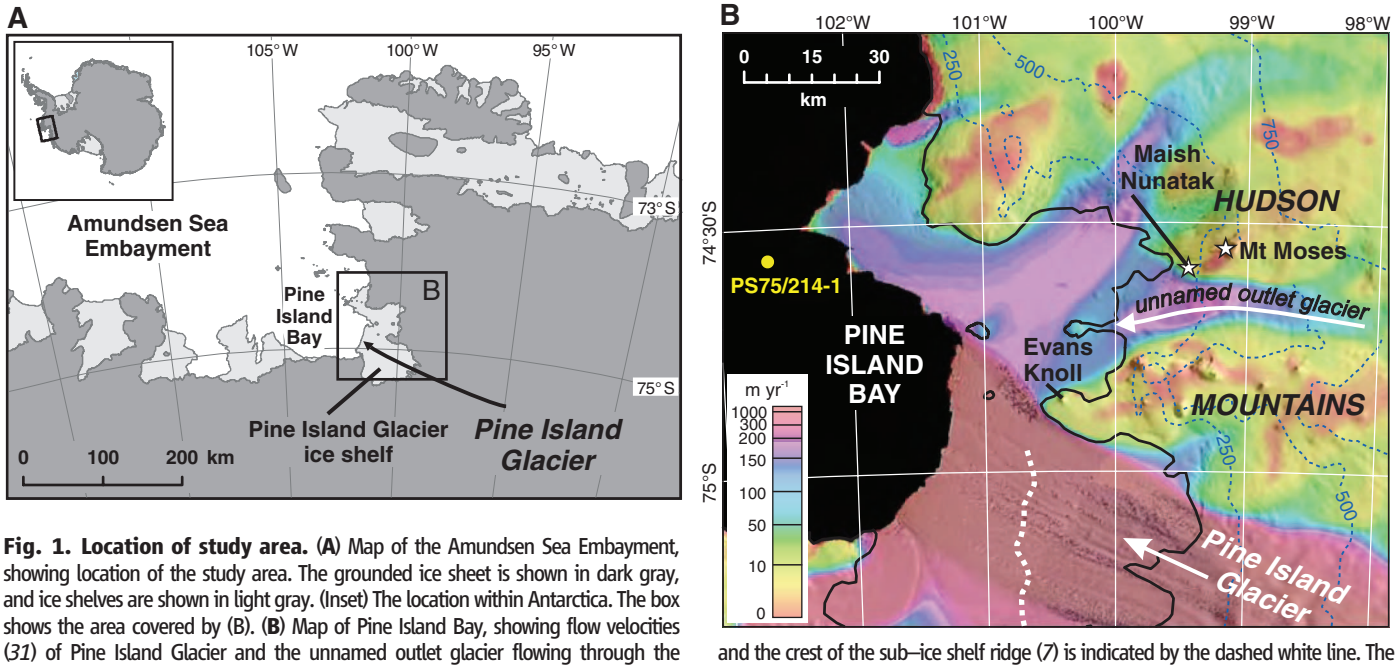

Fig. 1. Location of study area. (**A**) Map of the Amundsen Sea Embayment, showing location of the study area. The grounded ice sheet is shown in dark gray, and ice shelves are shown in light gray. (Inset) The location within Antarctica. The box shows the area covered by (B). (**B**) Map of Pine Island Bay, showing flow velocities (*31*) of Pine Island Glacier and the unnamed outlet glacier flowing through the Hudson Mountains, overlaid on Landsat Image Mosaic of Antarctica imagery (gray scale). Contours are in meters. The grounding line is indicated by the solid black line, and the crest of the sub–ice shelf ridge (*7*) is indicated by the dashed white line. The yellow circle indicates marine sediment core site PS75/214-1, which constrains grounding line retreat (before 11.7 ± 0.7 ka) from Pine Island Bay (*21*).